DART: Recent Advances in Remote Sensing Data Modeling With Atmosphere, Polarization, and Chlorophyll Fluorescence

Jean-Philippe Gastellu-Etchegorry, Nicolas Lauret, Tiangang Yin, Lucas Landier, Abdelaziz Kallel, Zbynek Malenovský, Ahmad Al Bitar, Josselin Aval, Sahar Benhmida, Jianbo Qi, Ghania Medjdoub, Jordan Guilleux, Eric Chavanon, Bruce Cook, Douglas Morton, Nektarios Chrysoulakis, and Zina Mitraka

***Abstract*—To better understand the life-essential cycles and processes of our planet and to further develop remote sensing (RS) technology, there is an increasing need for models that simulate the radiative budget (RB) and RS acquisitions of urban and natural landscapes using physical approaches and considering the three-dimensional (3-D) architecture of Earth surfaces. Discrete anisotropic radiative transfer (DART) is one of the most comprehensive physically based 3-D models of Earth-atmosphere radiative transfer, covering the spectral domain from ultraviolet to thermal infrared wavelengths. It simulates the optical 3-D RB and optical signals of proximal, aerial, and satellite imaging spectrometers and laser scanners, for any urban and/or natural landscapes and for any experimental and instrumental configurations. It is freely available for research and teaching activities. In this paper, we briefly introduce DART theory and present recent advances in simulated sensors (LiDAR and cameras with finite field of view) and modeling mechanisms (atmosphere, specular reflectance with polarization and chlorophyll fluorescence). A case study demonstrating a novel application of DART to investigate urban landscapes is also presented.**

***Index Terms*—Discrete anisotropic radiative transfer (DART), model, radiative transfer (RT), remote sensing.**

Manuscript received September 29, 2016; revised January 23, 2017; accepted March 8, 2017. Date of publication April 13, 2017; date of current version July 17, 2017. This work was supported by the Centre National d'Etudes Spatiales (CNES) in the frame of TOSCA projects 'Stem-Leaf' and 'Geostationary satellite' and by European Union's (EU) Horizon 2020 research and innovation program under grant agreement No 637519, project URBANFLUXES (http://urbanfluxes.eu/). Development of DART chlorophyll fluorescence modeling was supported by the NASA SIF funding: "Scaling Solar Induced Fluorescence from Leaves to Landscapes". *(Corresponding author: Tiangang Yin.)*

J.-P. Gastellu-Etchegorry, N. Lauret, L. Landier, A. Al Bitar, J. Aval, G. Medjdoub, J. Guilleux, and E. Chavanon are with the CESBIO - UPS, CNES, CNRS, IRD, Université de Toulouse, 31401 Toulouse Cedex 9, France (e-mail: jean-philippe.gastellu-etchegorry@cesbio.cnes.fr; nicolas.lauret@cesbio.cnes.fr; lucas.landier@cesbio.cnes.fr; ahmad.albitar@cesbio.cnes.fr; josselin.aval@gmail.com; medjdoub.ghania@gmail.com; guilleuxj@cesbio.cnes.fr; eric.chavanon@cesbio.cnes.fr).

T. Yin is with the CESBIO - UPS, CNES, CNRS, IRD, Université de Toulouse, 31401 Toulouse Cedex 9, France, and also with the CENSAM, Singapore-MIT Alliance for Research And Technology, 138602 Singapore (e-mail: tiangang.yin.85@gmail.com).

A. Kallel is with the CRNS, Technopark of Sfax, 3021 Sfax, Tunisia (e-mail: abdelaziz.kallel@enetcom.rnu.tn).

S. Benhmida is with the with the CESBIO - UPS, CNES, CNRS, IRD, Université de Toulouse, 31401 Toulouse Cedex 9, France, and also with the CRNS, Technopark of Sfax, 3021 Sfax, Tunisia (e-mail: sahar.ben.hmida@gmail.com).

J. Qi is with the CESBIO - UPS, CNES, CNRS, IRD, Université de Toulouse, 31401 Toulouse Cedex 9, France, and also with the College of Remote Science and Engineering, Beijing Normal University, Beijing 100875, China (e-mail: jianboqi@gmail.com).

Z. Malenovský, B. Cook, and D. Morton are with the NASA Goddard Space Flight Center and USRA-GESTAR, Greenbelt, MD 20771 USA (e-mail: zbynek.malenovsky@gmail.com; Bruce.Cook@nasa.gov; Douglas.Morton@nasa.gov).

N. Chrysoulakis and Z. Mitraka are with the Foundation for Research and Technology (FORTH), Heraklion 71110, Greece (e-mail: zedd2@iacm.forth.gr; zinoviam@gmail.com).

Color versions of one or more of the figures in this paper are available online at http://ieeexplore.ieee.org.

Digital Object Identifier 10.1109/JSTARS.2017.2685528

I. Introduction

SCIENTISTS, managers, and policy makers are increasingly using data from satellite and airborne optical sensors to study and manage forests, agricultural crops, as well as urban areas. This data, acquired with given technical specifications (spectral resolution, viewing direction, sensor field-of-view, etc.) and for a specific experimental configuration (surface/atmosphere conditions, sun direction, etc.), are commonly translated into qualitative and quantitative Earth surface parameters. However, atmosphere properties and three-dimensional (3-D) architecture of Earth surface objects often confound their interpretation. Hence, radiative transfer (RT) models that are able to simulate the Earth and atmosphere complexity are necessary tools for linking RS data with the Earth surface parameters. Presently, many RT models oversimplify radiation interaction in the Earth-atmosphere system, the simulation of landscapes, and the parameterization of sensor specifications as a tradeoff between model accuracy and operability. Hence, many efforts have been made by the scientific community to improve both components simultaneously. For example, the RAdiation transfer Model Intercomparison (RAMI) platform [1] was developed for testing and intercomparison of RT models. In the RAMI fourth phase, 12 RT models, including DART model [2], were tested. As expected, differences between model simulations were due to both 1) different mathematical approaches (Monte Carlo, etc.) and 2) 3-D representation of the considered vegetation landscapes.

This paper summarizes major aspects of DART and presents advances in present version 5.6.6 introduced since 2015, particularly: atmosphere RT, LiDAR, passive sensor with finite field of view (FOV), specular reflectance and polariza-

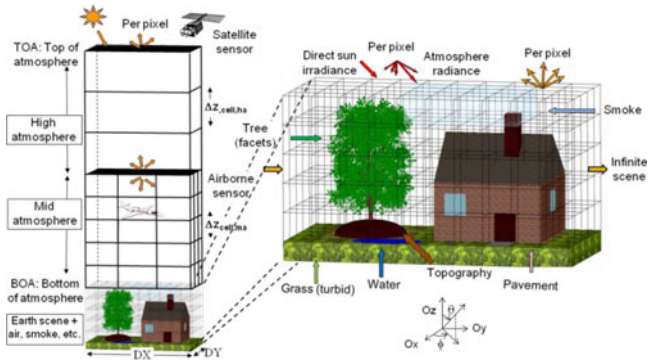

Fig. 1. Three-dimensional DART Earth/Atmosphere cell matrix scheme.

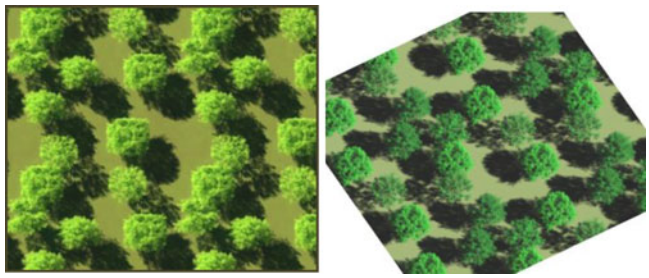

Fig. 2. DART simulated satellite image in natural colors: a virtual formation of citrus trees. Nadir (left) and oblique view (right).

tion, chlorophyll fluorescence, and DART calibration with multispectral satellite images.

II. DART Model

DART is being developed by the CESBIO Laboratory since 1992 and licenses are for research and teaching activities provided freely by the Paul Sabatier University (France) (www.cesbio.ups-tlse.fr/dart). Model accuracy was successfully tested for simulating vegetation canopy directional reflectance within RAMI experiments [1] and *in situ*/airborne comparisons [3], as well as brightness temperature at the bottom (BOA) and top (TOA) of the atmosphere [4]–[6]. DART is one of the most comprehensive physically based 3-D RT models. Compared to other models that participated in RAMI experiments (e.g., Drat [7], FLIGHT [8], RAYTRAN [9]), its application domain is broader. To our best knowledge, it is the only imaging RT model that works with the perspective projection, 3-D urban landscapes including relief topography, the atmosphere above and inside simulated scenes with spherical geometry covering the whole spectral domain from the ultraviolet up to thermal infrared (TIR) wavelengths. In addition, it can simulate any 3-D experimental combination of the Earth surface features (e.g., atmosphere, various forests, agricultural crops, date or sun direction, terrain geomorphology, etc.) and a high number of instrumental specifications (e.g., viewing directions, altitude, spatial and spectral resolutions, etc.) for imaging spectroradiometers and scanning LiDAR systems (discrete return, waveform, photon counting) aboard satellite/aircraft (e.g., ALS: Airborne Laser Scanner) or terrestrial platforms (e.g., TLS: terrestrial laser scanning). Additionally, the spatially explicit 3-D radiative budget (i.e., absorbed, emitted, scattered, and intercepted radiation) can be produced.

Several DART-specific functionalities can be briefly described as follows:

1) simulation of Earth surfaces and the atmosphere (see Fig. 1) with a dual approach: 3-D matrices of cells that contain turbid vegetation and/or fluids (gas, aerosol, water), with any distribution of facets, independently of the cell matrix geometry;
2) creation of its own 3-D scenes and import of standard geographical information (e.g., land cover map, 3-D urban model), or a combination of both;
3) simulation of foliar optical properties (OPs) with Prospect-4/5 [11] and Fluspect [12] models;
4) execution of sequences of simulations with varying any set of input parameters, for sensitivity studies and inversion approaches [13];
5) transformation of 3-D vegetation mock-ups that are built from geometrical facets into the turbid material (highly practical if the number of facets becomes too large);
6) reproduction of 3-D scenes that are infinite (i.e., spatially repetitive) with continuous relief, or finite for simulating small-scale indoor radiative measurements;
7) storage of results and input data (i.e., atmosphere and material spectra, atmosphere physical properties, etc.) in structured query language databases; and
8) multithreaded code for accelerating calculations executed through Python scripts and/or a graphic user interface (GUI).

DART is being used in numerous scientific applications such as: 1) inversion of RS images [13], [14]; 2) design of satellite sensors (e.g., LiDAR originally planned aboard NASA's DESDynI mission (https://decadal.gsfc.nasa.gov/DESDynI.html), high spatial resolution radiometer aboard the Pleiades mission of French Centre National d'Etudes Spatiales (https://pleiades.cnes.fr/) and various LiDAR missions [15]); 3) impact studies of canopy structure on satellite image texture [16] and reflectance [17]; 5) 3-D photosynthesis and primary production rates in vegetation canopies [18]; 5) design of a new chlorophyll index for evergreen conifer forests [19]; and 6) studies of tropical forest texture [20]–[22], among others.

Fig. 2 shows DART radiometer images of the citrus orchard created for the RAMI 4 experiment. Trees were provided as sets of facets and afterwards transformed into 3-D turbid cells. Simulations based on the tree facet and small-size turbid cells were found to be very similar, with reflectance root-mean-square error in the visible domain equal to 0.0023, for turbid cells of 20 cm.

III. Recent Advances in DART

A. Atmosphere

To provide an accurate radiative coupling between atmosphere and Earth surfaces, DART simulates the atmosphere RT using:

1) either direct input of gas / aerosol spectral scattering phase function, single-scattering albedo ω, and direct transmittance from BOA to TOA;
2) or derivation of gas/aerosol properties from a DART database that stores their vertical temperature/density/pressure profiles and direct transmittance (with 1 cm^{-1} spectral resolution). These data were derived from MODTRAN V5.2 [23], for six gas models (US Standard 1976, Tropical, Mid-Latitude Summer, Mid-Latitude Winter, Sub-Arctic Summer, and Sub-Arctic Winter) and six aerosol models (rural with a visibility V = 23 and 5 km, Maritime with V = 23 km, Urban with V = 5 km, Troposphere with V = 50 km, and Fog with V = 0.5 km).

For each gas model, DART database stores 14 absorbing gases (compared to 9 before 2015): uniformly mixed gases (CO_2, CH_4, CO, N_2O, and O_2), trace gases (NH_3, NO, NO_2, HNO_3, and SO_2), other dominant gases (H_2O, O_3, and N_2) and a gas that represents all other heavy gases. Each gas has a specific absorption cross-section spectrum that depends on its line-by-line nature and spectral broadening due to density, temperature, and pressure. Scattering gases are treated as a single gas since all of them obey the Rayleigh law over the spectrum. An optical depth, a single scattering albedo, and a scattering phase function simulated with a double Henyey–Greenstein function characterizes every aerosol type.

Fig. 3 shows DART and MODTRAN 5.2 TOA radiance/reflectance spectra with the 1 cm^{-1} wavenumber resolution in visible to shortwave infrared and TIR domains. For most wavelengths, especially in the so-called atmosphere windows, DART compares well with MODTRAN. Two reasons explain the bias in few DART-simulated TIR radiance values:

1) Limited accuracy in MODTRAN TIR transmittance that is stored only with four decimal digits. Hence, for some absorbing gases, the product of their cross-section and density per atmospheric layer gives a "0.0000" total transmittance in some wavelengths, which prevents to accurately specify the optical depth of atmosphere layers according to their density.
2) DART distributes gas optical depths, derived from transmittance, per atmosphere layer according to the gas density profile. This approach assumes a constant cross-section per gas type. Hence, it neglects the vertical variation of the cross-section with density, pressure, and temperature in each layer.

It should be noted that when simulating actual TIR acquisitions, these biases are partly mitigated, because bandwidths of RS sensors are relatively broad.

In addition to the updated atmosphere database, other functionalities were added in order to enable simulation of actual atmosphere configurations (e.g., urban pollution):

1) User specification of the amount of selected aerosols or gases, with the amount of the other ones being taken from the database.
2) User specification of atmosphere temperature at a given altitude. The associated temperature offset is calculated and applied to the vertical profile up to 20 km above the ground.

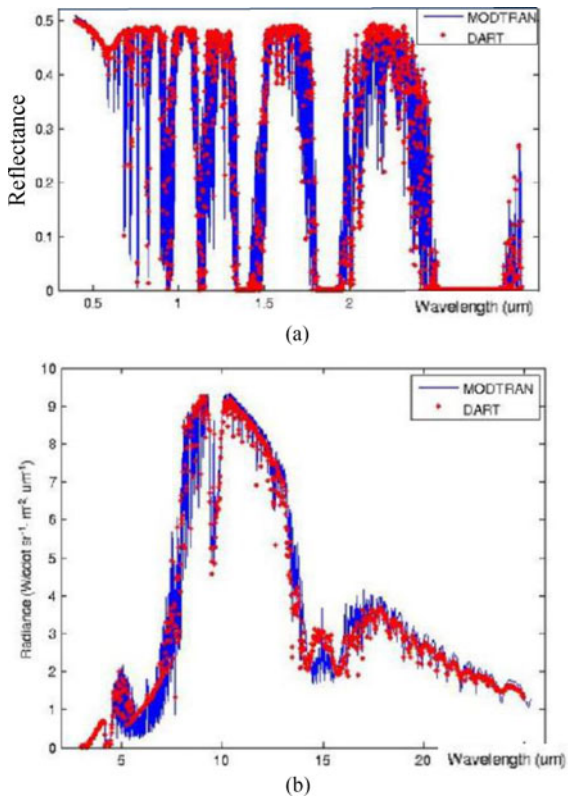

Fig. 3. DART versus MODTRAN 5.2 for an atmosphere defined by a US STD76 gas model and a rural V23 aerosol model. (a) TOA reflectance from the ultraviolet to the near-infrared domain (ground reflectance = 0.5). (b) TOA radiance in the thermal infrared domain (ground emissivity = 0.9).

3) Introduction of air within the Earth landscape. This is done using air cells that contain two mixed fluids with own OPs (i.e., spectral extinction coefficient, single scattering albedo, scattering phase function) that are exponential extensions of the atmosphere above the landscape. User can define any fluid OP.
4) Five-dimensional H_2O transmittance table in TIR as a function of distance, relative humidity, temperature, pressure, and wavelength. The table is used to correct atmosphere effects per pixel of ground-based TIR cameras. It considers the self and global line broadening and non-Beer law behavior of transmittance in spectral domains, where gas OPs have strong spectral variations.

B. LiDAR

LiDAR's fast development, especially in multibeam and scanning systems that launch pulses in many directions, requires efficient and accurate simulation tools to analyze existing data and to design future systems. Hence, DART was extended to model these systems [25], to import actual acquisition configurations and to export DART waveforms in a format accepted by a standard industrial LiDAR processing software. Fig. 4 shows a DART simulated ALS acquisition of Jarvselja pine stand in Estonia [26]. The simulation mimics the LiDAR aboard the CAO AtoMS system [27]. In the pine distribution scheme [see

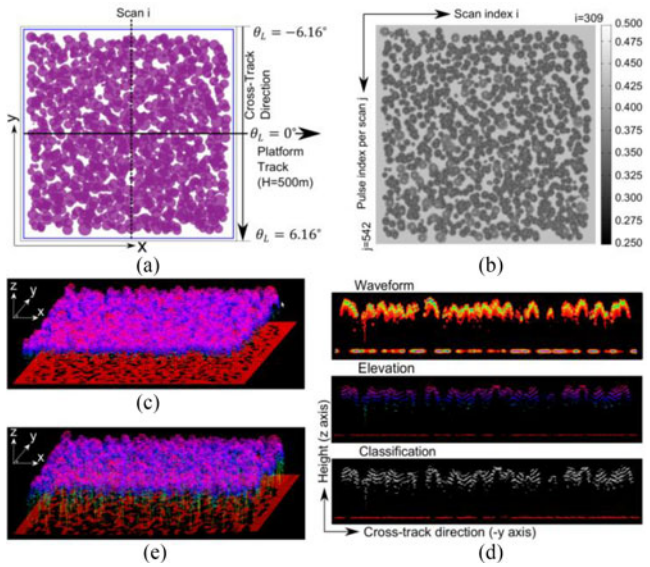

Fig. 4. ALS simulation. (a) Jarvselja pine stand and platform geometry (500-m altitude, zenith view angle θ_c from $-6.16°$ to $6.16°$. (b) Reflectance image per pulse. (c) Point cloud. (d) Points of scan i in (a). From top to bottom: waveform, elevation, ground classification (red: ground, white: no ground). (e) Same as (c) with $\theta_c = 45°$ at the swath center [25].

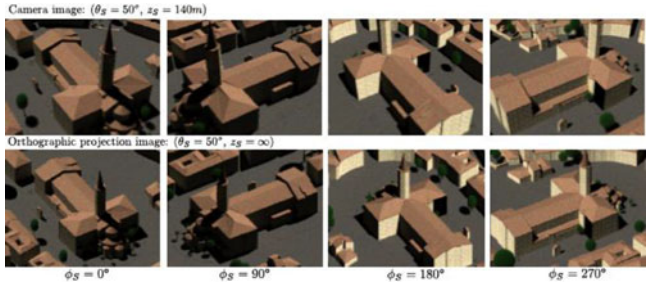

Fig. 5. DART satellite (top) and airborne (bottom) sensor images simulated in four viewing directions [29].

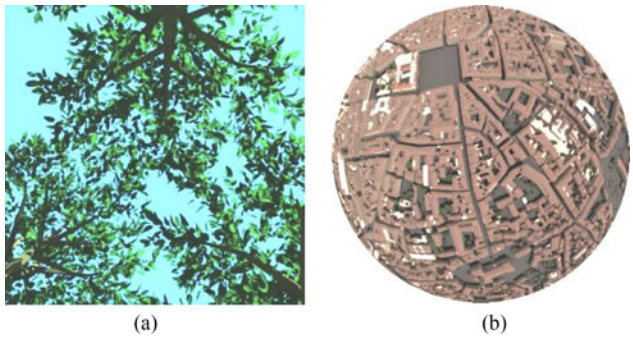

Fig. 6. Terrestrial sensor: upward (a) and downward (b) looking.

Fig. 4(a)], pines appear as circles with an area proportional to their crown size.

Fig. 4(b) presents the DART image of reflectance per pulse (i.e., ratio of backscattered and incident photons) and Fig. 4(c) shows the SPDlib processed point cloud after converting DART data into SPD format [28] with gain $g = 2.3\ 10^{-6}$ V/photon. Color indicates the local elevation. The ground signal is discontinued in case of pulses with no ground return. Fig. 4(d) illustrates three vertical sections for the scan with index i in Fig. 4(a), particularly waveform, elevation, and classification from top to bottom. Pine trunks give rise of only sparse returns, which is caused by the LiDAR central direction around nadir ($\theta_c \approx 0°$) allowing only few photons to reach them. As shown in Fig. 4(e), when simulating an oblique view ($\theta_c \approx 45°$), trunk returns appear clearly, while ground returns are reduced, as expected.

DART also simulates: 1) photon counting LiDAR, using single-photon detector physical principles and waveform simulation; 2) solar noise for any atmosphere by coupling simulation of LiDAR waveforms and passive sensor radiance images; and 3) TLS devices [25].

C. Airborne and Terrestrial Radiometers

Traditional RT models usually do not consider camera models and their image projection geometries (i.e., perspective projection for camera and/or parallel-perspective projection for cross-track imager), which is an important issue particularly for airborne sensors with a wide FOV. To simulate realistic images of Earth surfaces, as acquired by passive optical sensor with a finite FOV [29], 3-D perspective projection was introduced into DART to model the multidirectional acquisition within a given sensor FOV. During DART ray tracking, each passive sensor acquisition is simulated for the exact view direction from the scattering point to the sensor position, independently of the predefined DART discrete directions that track radiation along specific directions. With this new approach, DART can simulate cameras and cross-track imagers in most classical configurations. Fig. 5 shows DART satellite (parallel projection) and airborne (perspective projection) images of the Saint–Sernin basilica (Toulouse, France) in four view directions with 50° for zenith angle and four azimuth angles (0°, 90°, 180°, and 270°). The airborne sensor is placed 140 m above the ground. Size of the basilica tower is the same in all satellite images, but it varies on the four airborne images as the distance "airborne sensor—tower" varies with the camera position. This modeling method was also extended for simulating terrestrial imaging sensors. Fig. 6 shows an example of upward looking camera in a tree plot simulated with facets and a hemispherical camera looking downward over the Toulouse city center.

D. Specular Reflectance and Polarization

Many surfaces exhibit a specular reflection behavior. For example, measurements of a wheat canopy at 60° view zenith angle showed that blue sunlight that is specularly reflected can reach up to 35% of the total reflected light [30]. This ratio can be even much larger for water surfaces. Hence, vegetation foliage can appear white instead of green when viewed in the so-called sun specular direction. Conversely, to the unpolarized reflected diffuse light, the light of specular reflection does not enter the plant leaf interior. It is reflected and polarized by the first surface that intercepts it. When analyzing RS images, specular

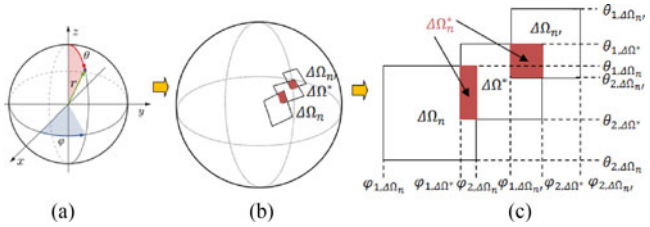

Fig. 7. (a) DART spherical coordinates. (b) Intersection of square solid angles of DART discrete directions $(\Omega_n,\ \Delta\Omega_n)$. Conical solid angles (not shown here) are also considered. (c) Solid angle $\Delta\Omega_n^*$ given by the intersection of the specular solid angle $\Delta\Omega^*$ and the DART discrete direction $(\Omega_n,\ \Delta\Omega_n)$.

and nonspecular radiation should be distinguished, because they bring different information about plant foliage components.

Surface specular reflectance and associated polarization effects are in DART modeled with Fresnel laws, taking into account the incident direction relative to the local surface normal and the roughness and refraction index of this surface. Specular reflectance modeling was introduced for both isotropic (Lambertian) and anisotropic (RPV [31] and Hapke [32]) surface reflectance models. Specular reflection is assumed to occur within a cone with a decreasing intensity from the cone central direction toward the cone boundary. A multiplicative factor, which is related to local roughness or other leaf characteristics, weights the Fresnel reflectance term. The so-called Stokes vector $\bar{S}$ represents polarization associated with specular reflectance. Hence, depending if polarization is simulated or not, DART works in a vector or a scalar mode. $\bar{S}$ is derived from the complex electric field $E(t)$. For a monochromatic plane, wave that propagates along the axis z_p, with {amplitude E, initial phase δ, frequency f, wave vector k} at time t and location z, we compute: $E(t) = E.e^{i(kz-2\pi ft+\delta)}$. Vector $\bar{S}$ is defined by the plane of polarization (x_P, y_P) in the polarization coordinate system $P(x_P, y_P, z_p)$ with $y_P \in (z_p, z)$, $y_P.z \geq 0$, $x_p \times y_p = z_p$ and $x_p.\ y_p = 0$. The coordinate system of the scattering plane is denoted as P-scat.

Specular intensity has to be computed for each DART discrete direction $(\Omega_n, \Delta\Omega_n)$. This computation relies on the intersection of the specular cone $\Delta\Omega^*$ with each defined direction $(\Omega_n, \Delta\Omega_n)$. Fig. 7 illustrates such computation, where $\Delta\Omega_n^*$ is the solid angle of the intersection.

From the receiver point of view, in polarization coordinate system P, the Stokes vector per discrete direction $(\Omega,\ \Delta\Omega)$ is noted

$$\bar{s}_{P,(\Omega,\Delta\Omega)} = \begin{pmatrix} I_P \\ Q_P \\ U_P \\ V_P \end{pmatrix}_P .$$

Hence, each DART vector source $W(r, \Omega)$ is a specific Stokes vector. Radiation interaction is modeled with Mueller matrices M (details are provided in the Annex). Fig. 8 shows drawing of the surface specular scattering mechanism, where incident direction zenith angle θ_{in} is equal to the incidence angle $\theta_{in\text{-}local}$ only for horizontal surfaces.

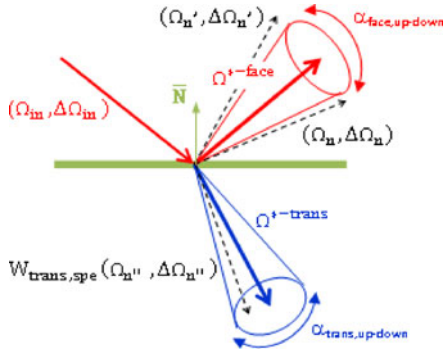

Fig. 8. Notations representing specular phenomena, with an incident direction $(\Omega_{in},\ \Delta\Omega_{in})$, DART discrete directions $(\Omega_n, \Delta\Omega_n)$, $(\Omega_{n'}, \Delta\Omega_{n'})$, and $(\Omega_{n''}, \Delta\Omega_{n''})$, specular directions Ω^{*face} and Ω^{*trans}, and an angular width of specular cones $\alpha_{face\ up\text{-}down}$ and $\alpha_{trans\ up\text{-}down}$.

Each interaction has three steps to transform $\bar{S}_{P,(\Omega_{in},\ \Delta\Omega_{in})}$:

$$\bar{S}_{P,(\Omega_{out},\Delta\Omega_{out})} = R_{P,(\Omega_{out},\Delta\Omega_{out})-scat\to P,(\Omega_{out},\Delta\Omega_{out})} . M . R_{P,(\Omega_{in},\Delta\Omega_{in})\to P,(\Omega_{in},\Delta\Omega_{in})-scat} . \bar{S}_{P,(\Omega_{in},\Delta\Omega_{in})} .$$

Step 1: Rotation of matrix $R_{P,(\Omega_{in},\Delta\Omega_{in})\to P,(\Omega_{in},\ \Delta\Omega_{in})-scat}$ transforms $\bar{S}_{P,(\Omega_{in},\ \Delta\Omega_{in})}$ into:

$$\bar{S}_{P,(\Omega_{in},\Delta\Omega_{in})-scat} = R_{P,(\Omega_{in},\Delta\Omega_{in})\to P,(\Omega_{in},\Delta\Omega_{in})-scat} \cdot \bar{S}_{P,(\Omega_{in},\Delta\Omega_{in})}$$

with $R_{P,(\Omega_{in},\Delta\Omega_{in})\to P,(\Omega_{in},\Delta\Omega_{in})-scat}$

$$= \begin{pmatrix} 1 & 0 & 0 & 0 \\ 0 & \cos 2\gamma_{P,(\Omega_{in},\Delta\Omega_{in})\to P,(\Omega_{in},\Delta\Omega_{in})-scat} & 0 & 0 \\ 0 & -\sin 2\gamma_{P,(\Omega_{in},\Delta\Omega_{in})\to P,(\Omega_{in},\Delta\Omega_{in})-scat} & 0 & 0 \\ 0 & 0 & 0 & 1 \end{pmatrix}$$

Step 2: The Mueller matrix M transforms $\bar{S}_{P,(\Omega_{in},\ \Delta\Omega_{in})-scat}$ into $\bar{S}_{P,(\Omega_{out},\ \Delta\Omega_{out})-scat} = M.\bar{S}_{P,(\Omega_{in},\ \Delta\Omega_{in})-scat}$.

Step 3: The rotation of matrix $R_{P,(\Omega_{out},\Delta\Omega_{out})\to P,(\Omega_{out},\Delta\Omega_{out})-scat}$ transforms $\bar{S}_{P,(\Omega_{out},\ \Delta\Omega_{out})-scat}$ into:

$$\bar{S}_{P,(\Omega_{out},\Delta\Omega_{out})} = R_{P,(\Omega_{out},\Delta\Omega_{out})-scat\to P,(\Omega_{out},\Delta\Omega_{out})} \cdot \bar{S}_{P,(\Omega_{out},\Delta\Omega_{out})-scat}$$

with $R_{P,(\Omega_{out},\Delta\Omega_{out})-scat\to P,(\Omega_{out},\Delta\Omega_{out})}$

$$= \begin{pmatrix} 1 & 0 & 0 & 0 \\ 0 & \cos -2\gamma_{P,(\Omega_{out},\Delta\Omega_{out})-scat\to P,(\Omega_{out},\Delta\Omega_{out})} & 0 & 0 \\ 0 & -\sin -2\gamma_{P,(\Omega_{out},\Delta\Omega_{out})-scat\to P,(\Omega_{out},\Delta\Omega_{out})} & 0 & 0 \\ 0 & 0 & 0 & 1 \end{pmatrix}$$

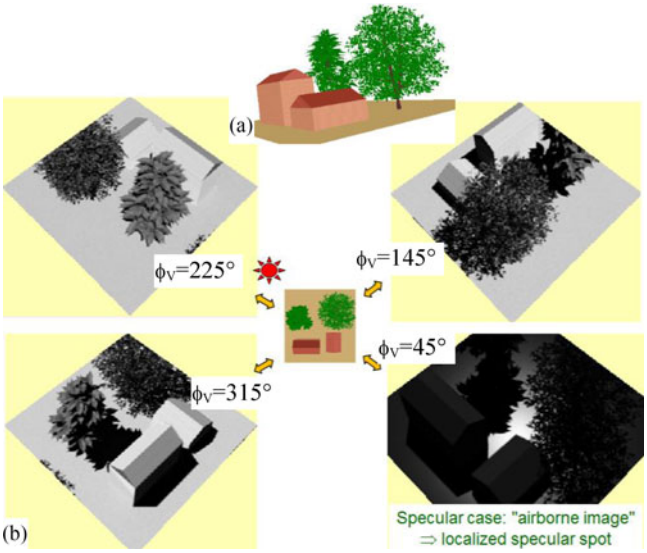

Fig. 9. Inundated scene with two houses and trees. (a) Scene 3-D representation. (b) Four DART airborne images (perspective projections) with the same zenith-viewing direction and four different azimuth-viewing angles. The bottom right pane shows the specular configuration.

Rotational angles $\gamma_{P,(\Omega_{in},\Delta\Omega_{in})\to P,(\Omega_{in},\Delta\Omega_{in})-scat}$ and $\gamma_{P,(\Omega_{out},\Delta\Omega_{out})-scat\to P,(\Omega_{out},\Delta\Omega_{out})}$ are defined with z-axis and the normal vectors $N_{(\Omega_{in},z)}$, $N_{(\Omega_{out},z)}$, and $N_{(\Omega_{in},\Omega_{out})}$) of planes (Ω_{in}, z), (Ω_{out}, z), and $(\Omega_{in}, \Omega_{out})$, respectively, as follows:

$$N_{(\Omega_{in},z)} = \frac{z \times \Omega_{in}}{|z \times \Omega_{in}|}, \quad N_{(\Omega_{out},z)} = \frac{z \times \Omega_{out}}{|z \times \Omega_{out}|},$$

$$\text{and } N_{(\Omega_{in},\Omega_{out})} = \frac{\Omega_{in} \times \Omega_{out}}{|\Omega_{in} \times \Omega_{out}|}.$$

If $z.N_{(\Omega_{in},\Omega_{out})} \geq 0$, then:

$$N_{(\Omega_{in},z)}.N_{(\Omega_{in},\Omega_{out})} = \cos\,\gamma_{P,(\Omega_{in},\Delta\Omega_{in})\to P,(\Omega_{in},\Delta\Omega_{in})-scat},$$

$$N_{(\Omega_{out},z)}.N_{(\Omega_{in},\Omega_{out})} = \cos\,\gamma_{P,(\Omega_{out},\Delta\Omega_{out})-scat\to P,(\Omega_{out},\Delta\Omega_{out})}.$$

If $z.N_{(\Omega_{in},\Omega_{out})} < 0$, then:

$$N_{(\Omega_{in},z)}.N_{(\Omega_{in},\Omega_{out})} = \cos\left(\pi - \gamma_{P,(\Omega_{in},\Delta\Omega_{in})\to P,(\Omega_{in},\Delta\Omega_{in})-scat}\right),$$

$$N_{(\Omega_{in},\Omega_{out})} = \cos\left(\pi - \gamma_{P,(\Omega_{out},\Delta\Omega_{out})-scat\to P,(\Omega_{out},\Delta\Omega_{out})}\right).$$

Fig. 9 shows four airborne images in perspective projections of a synthetic landscape: inundated ground surface with two houses and two trees. Central viewing directions are $\theta_v = 35°$ and $\phi_v = (45°, 135°, 225°, 315°)$ and the solar illumination direction is $\theta_{sun} = 35°$ and $\Phi_{sun} = 45°$. Specular reflectance appears only in a part of the image, where $\phi_v = 45°$. Ground roughness, sensor FOV, and sun radiation divergence define its spatial extent. It appears in the exact center of simulated airborne image only if ground surface is perfectly horizontal and smooth.

Depicting the same Earth scene as in Fig. 9, Fig. 10 illustrates the difference between DART simulations of satellite [see Fig. 10(a)–(c)] and airborne images [see Fig. 10(d)–(f)]. As an example, only part of the airborne image is in the specular configuration [see Fig. 10(f)] when compared to the satellite image of the same viewing geometry [see Fig. 10(c)].

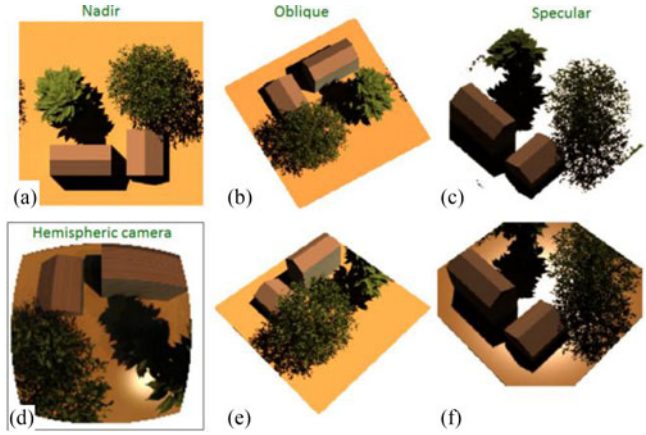

Fig. 10. Satellite and airborne images with DART simulated specular ground reflection. Top: satellite images (parallel projection) of three viewing directions: (a) nadir, (b) oblique off, (c) and along the specular direction. Bottom: aerial images (perspective projection) from (d) hemispherical camera, (e) oblique off, and along the (f) specular direction.

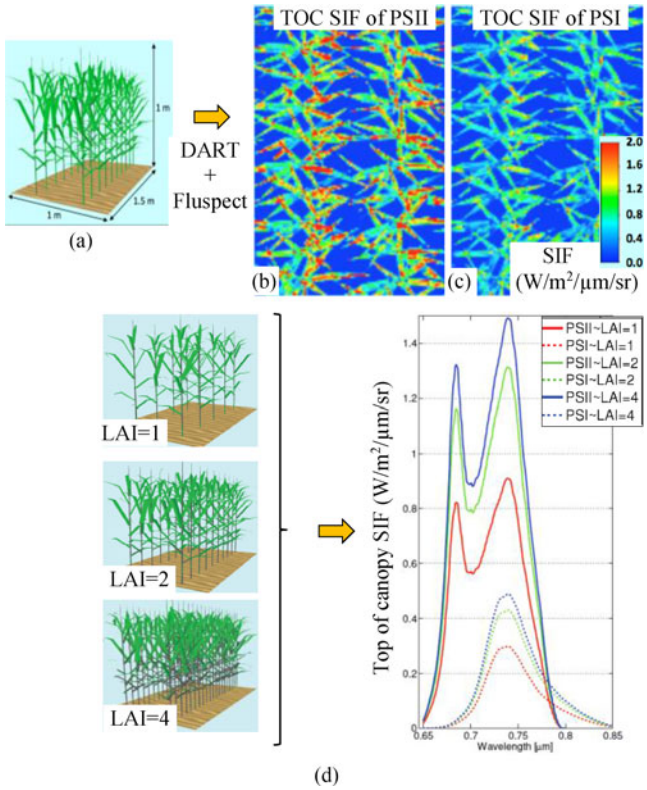

Fig. 11. Solar induced top-of-canopy chlorophyll fluorescence (sif). (a) Mid-season growth stage of maize (zea maise). Sif from photosystems I (b) and Ii (c) at 740 nm (1-nm band width, pixel size of 1 cm). (d) variation of sif with 3 LAI values (1, 2, 4).

Additionally, DART simulates images that correspond to the three polarization components (Q, U, and V) of vector $\bar{s}$ (results not shown).

E. Scaling Chlorophyll Fluorescence From Leaves to Canopies

A small fraction of excessive photosynthetically active radiation (PAR) absorbed by chlorophyll pigments of green plants is

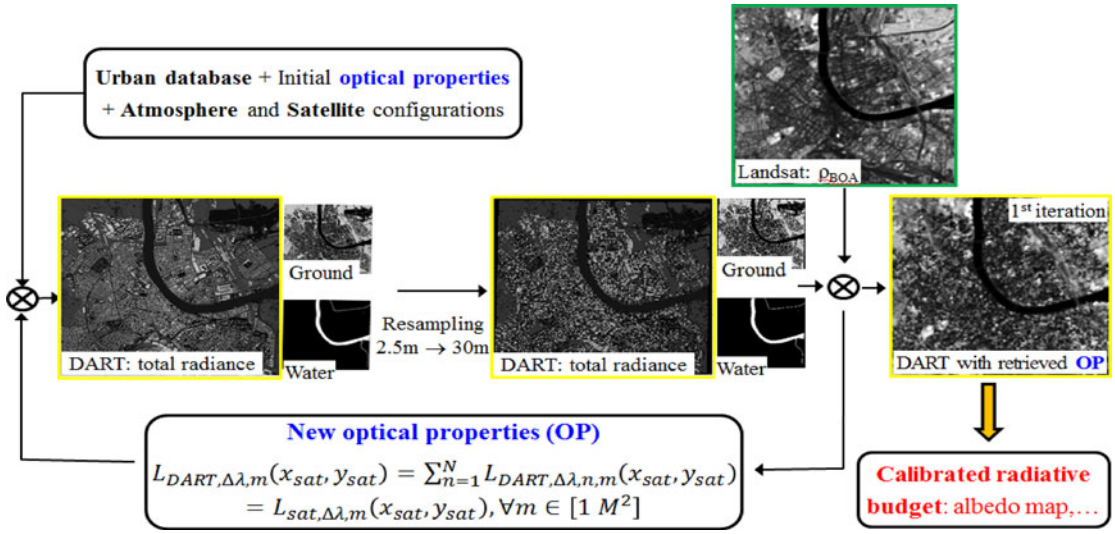

Fig. 12. Calibrating the urban radiative budget using satellite images. The OPs of urban surface material are derived per pixel of the available multispectral satellite image (in this case Landsat 8 ETM+).

re-emitted in longer wavelengths as fluorescence. The yield of solar induced chlorophyll fluorescence (SIF) is complementary to photosynthetic yield and heat dissipation as the remaining waste energy. SIF has been retrieved from various atmospheric satellite sensors, such as GOSAT, GOME-2, SCIAMACHY, and OCO-2 [34]. Although assimilation of the remotely sensed SIF data have improved modeling of vegetation gross primary production at global scale ([35], [36]), interpretation and use of SIF signal at local-to-regional scales need further understanding of SIF photon interactions with complex 3-D canopy structures. Hence, we enabled DART to simulate and upscale SIF emissions from leaves to complex plant canopies. For that:

1) Fluspect (B CX) RT model [12] that simulates leaf backward/forward fluorescence of photosystems one (PSI) and two (PSII), was implemented in DART, and
2) DART RT modeling was adapted to track fluorescent fluxes that originate from photosystems PSI and PSII.

The latest DART version simulates BOA and TOA SIF (640–850 nm) of any bandwidth, induced by light of PAR wavelengths (400–750 nm), for any canopy, terrain topography, atmosphere within and above the canopy, and other 3-D features of a landscape. DART sequences of RB simulations in 3-D canopies with, for instance, one hourly time steps, are used to discriminate sun and shade-adapted leaves. Fluorescence quantum yield efficiencies of both photosystems are specified on a leaf-by-leaf basis or per type of leaves. In the absence of a leaf photochemical model linked to DART RB simulation, the biologically correct parameterization of fluorescence inputs must be performed externally based on the standalone photosynthetic model, measurements or expert knowledge.

Fig. 11 shows simulated SIF signals, as if acquired and retrieved from an imaging spectrometer mounted on a tower 8 m over a maize (*Zea maise L.*) field. To carry out this simulation, the Fluspect model was parameterized with the OPs of a generic corn leaf provided in the PROSPECT-3 documentation [11]: leaf chlorophyll = 50 μg/cm^2, carotenoids = 15 μg/cm^2, water depth = 0.009 cm, dry matter = 0.0021 g/cm^2, and mesophyll structural parameter $N = 1.5$. Fluorescence quantum efficiency was set to 0.002 for PSI and 0.016 for PSII [37]. Fig. 11(b) and (c) show images of the simulated solar-induced top-of-canopy maize chlorophyll fluorescence in a steady state at 740 nm for PSII and PSI, respectively. We investigated changes in top-of-canopy SIF from chlorophyll pigments of both photosystems due to changes in canopy green biomass amount, i.e., increasing leaf area index (LAI). Fig. 11(d) shows a nonlinear increase in SIF with a linear increase of LAI values caused by higher scattering of SIF in near infrared and its reabsorption by chlorophylls in red wavelengths.

One should note that a single DART simulation provides full multiangular distribution of top-of-canopy SIF. Analysis of this distribution showed that canopy SIF of PSI and PSII is angularly anisotropic, similarly to reflectance and brightness temperature.

Although magnitude and spatial distribution of the simulated top-of-canopy fluorescence emissions are reasonable, comprehensive validation of the DART fluorescence modeling reliability, performed with real remotely sensed acquisitions, is still required.

F. Calibration of DART With Satellite Images

An innovative method was developed in the context of the H2020 project UrbanFluxes (http://urbanfluxes.eu/) for calibrating DART with satellite imagery. The OPs and temperature of the Earth surface material are determined per pixel from an optical (multispectral) satellite image. Method has been applied to three cities: Basel (Switzerland), Heraklion (Greece), and London (UK), using atmospherically corrected satellite images and 3-D city surface models (i.e., polygons defined as a list of vertices and texture vertices). The method (see Fig. 12) is iterative and has three major steps:

1) DART simulation of BOA radiance image at high spatial resolution (e.g., 0.5 m);
2) spatial resampling of DART images down to satellite spatial resolution (e.g., 10 m for Sentinel 2 and 30 m for Landsat 8); and
3) multiscale comparison of satellite and DART radiance to derive material OPs per satellite pixel.

The comparison uses variable numbers of neighbor satellite pixels in dependence on the number of urban elements in the pixel (i.e., roof, road, soil, vegetation). If DART radiance does not match the satellite image radiance, then the method starts new iteration (step 1).

First results are highly encouraging, indicating that DART and satellite images fit well. The retrieved (satellite calibrated) OPs lead to "DART—Landsat 8" pixel relative radiance differences smaller than 5%. This good fit allowed fulfilling the objective of the project, i.e., to get an accurate 3-D urban RB (albedo and exitance images in the visible and TIR domains). This outcome can be attributed to the capability of DART to simulate accurately radiance values in all directions of the upper hemisphere. The UrbanFluxes project uses the DART simulated RB to model the urban energy budget, in order to derive urban anthropogenic heat fluxes from Earth observation Satellites. To achieve this objective, DART computes time variations of urban RB using multispectral satellite time series.

IV. Conclusion

DART modeling algorithm and functions are continuously improved by research and computer scientists of CESBIO in collaboration with research scientists from other laboratories of several countries (USA, Singapore, Tunisia, China, Switzerland, Czech Republic, etc.). This paper presents recent improvements in modeling physical (atmosphere RT and specular interaction with polarization) and biophysical vegetation processes (fluorescence), and also in simulating the observation of satellite, airborne and terrestrial LiDARs, and spectroradiometers with finite FOV. It also presents an innovative method for detection and parameterization of OPs of Earth materials directly from multispectral satellite images. It should be mentioned that fluorescence modeling takes advantage of the nonremote sensing DART component (i.e., the simulation of 3-D RB). These improvements open new scientific possibilities: 1) The simulation of RS sensors in presence of urban pollution can be carried out with a higher precision thanks to the new atmosphere RT modeling. 2) The analysis of airborne sensor observations, and even Earth satellite observations, has improved based on modeling of sensors with finite FOV. 3) Effects of a vegetation 3-D architecture on LiDAR signals and SIF can be efficiently assessed using new LiDAR and fluorescence modeling tools. This is important especially for local-to-regional SIF observations, since the state-of-the-art fluorescence models such as the soil-canopy integrated SCOPE model [12] are 1-D models. 4) Survey of landscape albedo using satellite time series, driven by introduction of surface element OPs that vary per satellite pixel.

Some of the aforementioned DART improvements still need thorough validation for operational purposes. One should note that all improvements are aimed to be as much as feasible coherent. For example, regardless the spectral domain and the application domain (i.e., simulation of RB and/or any RS sensor) DART works with the same representation of atmosphere and urban/vegetation landscapes. This is important for studies on the fusion of acquisitions from different types of remote sensing sensors.

DART is being continuously improved in terms of physics, computational performance, and new functions. Major on-going and planned work is listed below:

1) Two approaches are investigated for simulating scenes with larger spatial dimensions. a) Subdivision of the scene as a finite number of subscenes, when each subscene provides radiation boundary conditions to its neighboring subscenes. b) Consideration of cells with different dimensions in the same landscape simulation. This is a classical computer graphic method. It is expected that both approaches will strongly decrease computational time and computer storage requirements, which will allow simulations of spatially extensive scenes.
2) RT modeling in water bodies, as an extension of DART RT modeling in fluids, including the light refraction mechanism.
3) Chlorophyll fluorescence modeling in 3-D turbid media vegetation canopies including nonphotosynthetic woody surfaces (trunks, branches, and twigs).
4) Creation of a new user-friendly GUI in accordance with the latest computer science standards.

Throughout 20 years of development, DART has reached the stage of a reference RT model in the field of optical RS, both for LiDAR and spectral systems.

ANNEX

A few examples of Mueller matrices modeling specular reflection in DART are shown below.

Mueller matrix is written as $M = \mathrm{s}.M_r$, where s is an unpolarized term that represents the interaction with an unpolarized input radiation and M_r is the reduced mueller matrix of this interaction.

1) *Fresnel reflection:*

$$s = r^2\left(\theta_{\mathrm{in-local}}\right) \text{ with } I_{P,(\Omega_{\mathrm{out}},\Delta\Omega_{\mathrm{out}})}$$
$$= r^2\left(\theta_{\mathrm{in-local}}\right).I_{P,(\Omega_{\mathrm{in}},\Delta\Omega_{\mathrm{in}})}$$
$$\text{with } r^2\left(\theta_{\mathrm{in-local}}\right) = \frac{r^2_{\mathrm{x}_{\mathrm{P},(\Omega_{\mathrm{in}},\Delta\Omega_{\mathrm{in}})-\mathrm{scat}}} + r^2_{\mathrm{y}_{\mathrm{P},(\Omega_{\mathrm{in}},\Delta\Omega_{\mathrm{in}})-\mathrm{scat}}}}{2}$$
$$\text{and } Q_{P,(\Omega_{\mathrm{in}},\Delta\Omega_{\mathrm{in}})} = U_{P,(\Omega_{\mathrm{in}},\Delta\Omega_{\mathrm{in}})} = V_{P,(\Omega_{\mathrm{in}},\Delta\Omega_{\mathrm{in}})} = 0.$$

Fresnel coefficients $r^2_{\mathrm{x}_{\mathrm{P},(\Omega_{\mathrm{in}},\Delta\Omega_{\mathrm{in}})-\mathrm{scat}}}$ and $\mathrm{r}^2_{\mathrm{y}_{\mathrm{P},(\Omega_{\mathrm{in}},\Delta\Omega_{\mathrm{in}})-\mathrm{scat}}}$ depend on $\theta_{\mathrm{in-local}}$. $\mathrm{r}^2_{\mathrm{x}_{\mathrm{P},(\Omega_{\mathrm{in}},\Delta\Omega_{\mathrm{in}})-\mathrm{scat}}}$ are applied to rays with perpendicular polarization (i.e., $\frac{Q_{P,(\Omega_{\mathrm{in}},\Delta\Omega_{\mathrm{in}})-\mathrm{scat}}}{I_{P,(\Omega_{\mathrm{in}},\Delta\Omega_{\mathrm{in}})-\mathrm{scat}}} = 1$), shown in equation on the top of the next page.

$r^2_{\mathrm{y}_{\mathrm{P},(\Omega_{\mathrm{in}},\Delta\Omega_{\mathrm{in}})-\mathrm{scat}}}$ is applied to rays with parallel polarization (i.e., $\frac{Q_{P,(\Omega_{\mathrm{in}},\Delta\Omega_{\mathrm{in}})-\mathrm{scat}}}{\mathrm{I}_{P,(\Omega_{\mathrm{in}},\Delta\Omega_{\mathrm{in}})-\mathrm{scat}}} = -1$), shown in equation on the top of the next page.

$$\mathrm{M_r} = \begin{pmatrix} 0 & \frac{r^2_{x_{P,(\Omega_{in},\Delta\Omega_{in})-scat}} - r^2_{y_{P,(\Omega_{in},\Delta\Omega_{in})-scat}}}{r^2_{x_{P,(\Omega_{in},\Delta\Omega_{in})-scat}} + r^2_{y_{P,(\Omega_{in},\Delta\Omega_{in})-scat}}} & 0 & 0 \\ \frac{r^2_{x_{P,(\Omega_{in},\Delta\Omega_{in})-scat}} - r^2_{y_{P,(\Omega_{in},\Delta\Omega_{in})-scat}}}{r^2_{x_{P,(\Omega_{in},\Delta\Omega_{in})-scat}} + r^2_{y_{P,(\Omega_{in},\Delta\Omega_{in})-scat}}} & 1 & 0 & 0 \\ 0 & 0 & \frac{2.r^2_{x_{P,(\Omega_{in},\Delta\Omega_{in})-scat}}.r^2_{y_{P,(\Omega_{in},\Delta\Omega_{in})-scat}}}{r^2_{x_{P,(\Omega_{in},\Delta\Omega_{in})-scat}} + r^2_{y_{P,(\Omega_{in},\Delta\Omega_{in})-scat}}} & 0 \\ 0 & 0 & 0 & \frac{2.r^2_{x}.r^2_{y_{P,(\Omega_{in},\Delta\Omega_{in})-scat}}}{r^2_{x_{P,(\Omega_{in},\Delta\Omega_{in})-scat}} + r^2_{y_{P,(\Omega_{in},\Delta\Omega_{in})-scat}}} \end{pmatrix}$$

Fresnel refraction Mueller matrix is similar: $r^2_{x_P}$ and $r^2_{y_P}$ are replaced by $t^2_{x_P}$ and $t^2_{y_P}$

2) *Rayleigh and Mie scattering:*

The un-polarized term $s = s(\Psi)_{\text{Rayleigh or Mie}}$ defined by:

$$I_{P,(\Omega_{out},\Delta\Omega_{out})} = s(\Psi).I_{P,(\Omega_{in},\Delta\Omega_{in})} \text{ and}$$

$$Q_{P,(\Omega_{in},\Delta\Omega_{in})} = U_{P,(\Omega_{in},\Delta\Omega_{in})} = V_{P,(\Omega_{in},\Delta\Omega_{in})} = 0$$

$$\mathrm{M}_r = \begin{pmatrix} 1 & \frac{1-\cos^2\Psi}{1+\cos^2\Psi} & 0 & 0 \\ \frac{1-\cos^2\Psi}{1+\cos^2\Psi} & 1 & 0 & 0 \\ 0 & 0 & \frac{2\cos\Psi}{1+\cos^2\Psi} & 0 \\ 0 & 0 & 0 & \frac{2\cos\Psi}{1+\cos^2\Psi} \end{pmatrix}_{\text{Rayleigh}}$$

$$\mathrm{M}_r = \begin{pmatrix} 1 & \mathrm{M}_{12}(\Psi) & 0 & 0 \\ \mathrm{M}_{12}(\Psi) & 1 & 0 & 0 \\ 0 & 0 & \mathrm{M}_{33}(\Psi) & 0 \\ 0 & 0 & 0 & \mathrm{M}_{33}(\Psi) \end{pmatrix}_{\text{Mie}}.$$

For nonspherical randomly oriented particles, the general expression of the Mueller matrix is:

$$\mathrm{M} = \begin{pmatrix} \mathrm{M}_{11} & \mathrm{M}_{12} & 0 & 0 \\ \mathrm{M}_{12} & \mathrm{M}_{22} & 0 & 0 \\ 0 & 0 & \mathrm{M}_{33} & \mathrm{M}_{34} \\ 0 & 0 & -\mathrm{M}_{34} & \mathrm{M}_{44} \end{pmatrix}.$$

ACKNOWLEDGMENT

The authors are grateful to Toulouse town hall for providing the Toulouse city geo-database and thankful to all scientists who contributed to DART development since its first step in 1992.

REFERENCES

[1] J. L. Widlowski *et al.*, "The 4th phase of the radiative transfer model intercomparison exercise: Actual canopy scenarios and conformity testing," *Remote Sens. Environ.*, vol. 169, pp. 418–437, 2015.

[2] J. P. Gastellu-Etchegorry *et al.*, "Discrete anisotropic radiative transfer (DART 5) for modelling airborne and satellite spectroradiometer and LiDAR acquisitions of natural and urban landscapes," *Remote Sens.*, vol. 7, no. 2, pp. 1667–1701, 2015.

[3] J. P. Gastellu-Etchegorry *et al.*, "Modeling BRF and radiation regime of boreal and tropical forests: I. BRF," *Remote Sens. Environ.*, vol. 68, no. 3, pp. 281–316, 1999.

[4] P. Guillevic, J. P. Gastellu-Etchegorry, J. Demarty, and L. Prévot, "Thermal infrared radiative transfer within 3-D vegetation cover," *J. Geophys. Res.—Atmosphre*, vol. 108, 2003, doi: 10.1029/2002JD002247.

[5] P.C. Guillevic *et al.*, "Directional viewing effects on satellite Land Surface Temperature products over sparse vegetation canopies—A multi-sensor analysis," *IEEE Geosci. Remote Sens.*, vol. 10, no. 6, pp. 1464–1468, Nov. 2013.

[6] J. A. Sobrino, C. Mattar, J. P. Gastellu-Etchegorry, J. C. Jimenez Munoz, and E. Grau, "Evaluation of the DART 3D model in the thermal domain using satellite/airborne imagery and ground-based measurements," *Int. J. Remote Sens.*, vol. 32, pp. 7453–7477, 2011, doi:10.1080/01431161.2010.524672.

[7] M. I. Disney, P. Lewis, and P. R. J. North, "Monte Carlo ray tracing in optical canopy reflectance modelling," *Remote Sens. Rev.*, vol. 18, nos. 2–4, pp. 163–196, 2000.

[8] P. North, "Three-dimensional forest light interaction model using a Monte Carlo method," *IEEE Trans. Geosci. Remote Sens.*, vol. 34, no. 4, pp. 946–956, Jul. 1996.

[9] Y. M. Govaerts and M. M. Verstraete, "Raytran: A Monte Carlo ray-tracing model to compute light scattering in three-dimensional heterogeneous media," *IEEE Trans. Geosci. Remote Sens.*, vol. 36, no. 2, pp. 493–505, Mar. 1998.

[10] E. Grau and J.-P. Gastellu-Etchegrry, "Radiative transfer modeling in the 'Earth—Atmosphere' system with DART model," *Remote Sens. Environ.*, vol. 139, pp. 149–170, 2013.

[11] S. Jacquemoud and F. Baret, "Prospect—A model of leaf optical properties spectra," *Remote Sens. Environ.*, vol. 34, pp. 75–91, 1990.

[12] C. van der Tol, W. Verhoef, J. Timmermans, A. Verhoef, and Z. Su, "An integrated model of soil-canopy spectral radiances, photosynthesis, fluorescence, temperature and energy balance," *Biogeoscience*, vol. 6, no. 12, pp. 3109–3129, 2009.

[13] A Banskota *et al.*, "Investigating the utility of wavelet transforms for inverting a 3-D radiative transfer model using hyperspectral data to retrieve forest LAI," *Remote Sens.*, vol. 5 no. 6, pp. 2639–2659. 2013.

[14] F. Gascon, J. P. Gastellu-Etchegorry, M. J. Lefevre, and E. Dufrene, "Retrieval of forest biophysical variables by inverting a 3-D radiative transfer model and using high and very high resolution imagery," *Int. J. Remote Sens.*, vol. 25, no. 24, pp. 5601–5616. 2004.

[15] S. Durrieu *et al.*, "Preliminary studies for a vegetation ladar/LiDAR space mission in France," in *Proc. IEEE Int. Geosci. Remote Sens. Symp.*, Melbourne, Vic., Australia, 2013, pp. 2332–2335.

[16] V. Bruniquel-Pinel and J. P. Gastellu-Etchegorry, "Sensitivity of texture of high resolution images of forest to biophysical and acquisition parameters," *Remote Sens. Environ.*, vol. 65, no. 1, pp. 61–85, 1998.

[17] Z. Malenovský *et al.*, "Influence of woody elements of a Norway spruce canopy on nadir reflectance simulated by the DART model at very high spatial resolution," *Remote Sens. Environ.*, vol. 112, no. 1, pp. 1–18. 2008.

[18] P. Guillevic and J. P. Gastellu-Etchegorry, "Modeling BRF and radiation regime of boreal and tropical forest: II. PAR regime," *Remote Sens. Environ.*, vol. 68, no. 3, pp. 317–340, 1999.

[19] Z. Malenovský *et al.*, "Retrieval of spruce leaf chlorophyll content from airborne image data using continuum removal and radiative transfer," *Remote Sens. Environ.*, vol. 131, pp. 85–102, 2013.
[20] N. Barbier, P. Couteron, C. Proisy, Y. Malhi, and J. P. Gastellu-Etchegorry, "The variation of apparent crown size and canopy heterogeneity across lowland Amazonian forests," *Glob. Ecol. Biogeography*, vol. 19, no. 1, pp. 72–84, 2010.
[21] N. Barbier, P. Couteron, J. P. Gastelly-Etchegorry, and C. Proisy, "Linking canopy images to forest structural parameters: Potential of a modeling framework," *Ann. Forest Sci.*, vol. 69, no. 2, pp. 305–311, 2012.
[22] C. Proisy *et al.*, 2016, "Biomass prediction in tropical forests: The canopy grain approach," in *Remote Sensing of Biomass: Principles and Applications*. Rijeka, Croatia: InTech Publisher, 2011, pp. 1–18.
[23] A. Berk, "MODTRAN band model transmittance," *Rpt. SSI-SR*, vol. 69, pp. 1–11, 1996.
[24] J. P. Gastellu-Etchegorry *et al.*, "Simulation of LiDAR acquisition in Earth-Atmosphere system with DART model (I): Waveform simulation with a pseudo-Monte Carlo ray tracing mode," *Remote Sens. Environ.*, vol. 184, pp. 418–435, 2016.
[25] T. Yin, N. Lauret, and J.P. Gastellu-Etchegorry, "Simulation of satellite, airborne and terrestrial LIDAR with DART model (II): Multi-pulse devices, photon counting, and solar noise," *Remote Sens. Environ.*, vol. 184, pp. 454–468, 2016.
[26] A. Kuusk, J. Kuusk, and M. Lang, "A dataset for the validation of reflectance models," *Remote Sens. Environ.*, vol. 113, pp. 889–892. 2009.
[27] G.P. Asner, *et al.*, "Carnegie Airborne Observatory-2: Increasing science data dimensionality via high-fidelity multi-sensor fusion,". *Remote Sens. Environ.*, 124, pp. 454–465, 2012.
[28] P. Bunting, J. Armston, R. M. Lucas, and D. Clewley, "Sorted Pulse Data (SPD) Library. Part I: A generic file format for LiDAR data from pulsed laser systems in terrestrial environments," *Comput. Geosci.*, vol. 56, pp. 197–206. 2013.
[29] T. Yin, N. Lauret, and J.-P. Gastellu-Etchegorry, "Simulating images of passive sensors with finite field of view by coupling 3-D radiative transfer model and sensor perspective projection," *Remote Sens. Environ.*, vol. 162, pp. 169–185. 2015.
[30] VC Vanderbilt and L Grant. "Plant canopy specular reflectance model," *IEEE Trans. Geosci. Remote Sens.*, vol. 23, no. 5, pp. 722–730, 1985.
[31] H. Rahman, M. M. Verstraete, and B. Pinty, "Coupled surface-atmosphere reflectance (CSAR) model. 1. Model description and inversion on synthetic data," *J. Geophys. Res.*, vol. 98, no. 20, pp. 779-20,789. 1993.
[32] B. W. Hapke, "Bidirectional reflectance spectroscopy: 1. Theory," *J. Geophys. Res.*, vol. 86, pp. 3039–3054, 1981.
[33] T. Nilson and A. Kuusk, "A reflectance model for the homogeneous plant canopy and its inversion," *Remote Sens. Environ.*, vol. 27, pp. 157–167. 1989.
[34] L. Guanter *et al.*, "Estimation of solar-induced vegetation fluorescence from space measurements," *Geophys. Res. Lett.*, vol. 34, p. L08401. 2007.
[35] L. Guanter *et al.*, "Global and time-resolved monitoring of crop photosynthesis with chlorophyll fluorescence," *Proc. Nat. Acad. Sci. USA*, vol. 111, no. 14, pp. E1327–E1333, 2014.
[36] J. Joiner *et al.*, "The seasonal cycle of satellite chlorophyll fluorescence observations and its relationship to vegetation phenology and ecosystem atmosphere carbon exchange," *Remote Sens. Environ.*, vol. 152, pp. 375–391. 2014.
[37] A. Rosema, J. F. H. Snel, H. Zahn, W. F. Buurmeijer, and L. W. A. Van Hove, "The relation between laser-induced chlorophyll fluorescence and photosynthesis," *Remote Sens. Environ.*, vol. 65, no. 2, pp. 143–154. 1998.

Authors' photographs and biographies not available at the time of publication.